PHYSICAL REVIEW E **92**, 022211 (2015)

Shear-induced segregation of particles by material density

Yi Fan
The Dow Chemical Company, Midland, Michigan 48667, USA

K. M. Hill[*]
St. Anthony Falls Laboratory, Department of Civil Engineering, University of Minnesota, Minneapolis, Minnesota 55414, USA

(Received 8 June 2015; published 25 August 2015)

Recently, shear rate gradients and associated gradients in velocity fluctuations (e.g., granular temperatures or kinetic stresses) have been shown to drive segregation of different-sized particles in a manner that reverses at relatively high solids fractions ($\langle f \rangle > 0.50$). Here we investigate these effects in mixtures of particles differing in material density through computational and theoretical studies of particles sheared in a vertical chute where we vary the solids fraction from $\langle f \rangle = 0.2$ to 0.6. We find that in sparse flows, $\langle f \rangle = 0.2$ to 0.4, the heavier (denser) particles segregate to lower shear rates similarly to the heavier (larger) particles in mixtures of particles differing only in size. However, *there is no segregation reversal* at high f in mixtures of particles differing in density. At all solids fractions, heavier (denser) particles segregate to regions of lower shear rates and lower granular temperatures, in contrast with segregation of different-sized particles at high f, where the heavier (larger) particles segregate to the region of higher shear rates. Kinetic theory predicts well the segregation for both types of systems at low f but breaks down at higher f's. Our recently proposed mixture theory for high f granular mixtures captures the segregation trends well via the independent partitioning of kinetic and contact stresses between the two species. In light of these results, we discuss possible directions forward for a model framework that encompasses segregation effects more broadly in these systems.

DOI: 10.1103/PhysRevE.92.022211 PACS number(s): 81.05.Rm, 47.57.Gc

I. INTRODUCTION

Granular materials tend to segregate when particles in the mixture differ in size, material density, shape, or other properties. Segregation due to differences only in material density (often called *density segregation*, e.g., Refs. [1–3]) has wide implications for a variety of natural and industrial processes. For example, in a vibrofluidized bed, density difference between an impurity and the rest of the particles in the bed creates problems for a variety of processes employing this mechanism for transport (e.g., Ref. [4]). In longitudinal bars of braided rivers, this segregation can give rise to local accumulations of economically important denser materials (e.g., gold, uranium, and diamonds) due to the separation of these minerals from particles that are less dense (e.g., sand and gravel) [5]. The implications of segregation for geomorphological issues are even broader, as evidence points to the influence of local variation of particle density on local variability of erosion rates [6] and sediment transport rates [7] compared to expected rates (e.g., Ref. [8]).

Segregation according to particle density has been studied experimentally and computationally under a variety of boundary conditions and methods of excitation, including vibrated systems [2–4,9] and sheared systems such as gravity-driven flows in rotating drums [10–15] and down-inclined planes [16], and shear bands in split-bottom cells [17]. In vibrated systems, several factors have been shown to play important roles in the segregation process, including convection [1], gravity [4], interstitial air [9], and granular temperature (essentially, the kinetic energy associated with velocity variances) [1,18]. In sheared flows, similar mechanisms have been shown to influence the segregation processes, including variations in particle concentration (e.g., Refs. [17,19]). In this paper, we distinguish between segregation according to "particle density" (the focus of this paper) and segregation associated with variations of "concentration," or solids fractions by restricting our use of the words "dense" and "less dense" to refer to the material density of the particles ρ_m and use phrases such as "high or low concentrations" (or "sparse flows") to refer to relative solids fractions f.

In sparse sheared flows, kinetic theory (e.g., Refs. [20–23]) has been used successfully to model and predict segregation in simulations [20] and experiments [24]. The segregation predictions may represent segregation according to several competing elements: gravity, granular temperature, pressure, and diffusion "forces" (e.g., Refs. [20,22,23]). For example, gravity segregates denser particles downward (in the direction of gravity) relative to less dense particles (e.g., Ref. [23]) while a gradient of granular temperature segregates denser particles to lower granular temperature (e.g., Refs. [20,21]). For low-to-moderate system-averaged solids fractions ($\langle f \rangle$ up to 0.4), kinetic theory predicts segregation trends well [25]. Kinetic theory has been shown to be similarly effective in predicting segregation by temperature gradient in mixtures of different-sized particles at low-to-moderate f's [25,26], where the heavier (larger) particles also segregate to regions of lower temperature. However, as we detail shortly, for sufficiently high f's, we have shown that for particles of different sizes, the segregation reverses, that is, heavier (larger) particles segregate to regions of higher shear rates and higher granular temperatures [17,26], a phenomenon kinetic theory fails to capture. These trends at high f have not been investigated for segregation of particles differing in material density.

---

[*] kmhill@umn.edu

In most studies of sheared systems of relatively high system-averaged solids fractions $\langle f \rangle$, the primary focus of segregation of granular mixtures has involved the effect of gravity, while the effect of granular temperature has not been thoroughly explored. Typically, in high-f flows, similarly to sparse flows, denser particles sink relative to equal-sized lighter neighbors, and less dense particles rise. In high-f flow, Khakhar *et al.* [10] proposed a "buoyancy" mechanism, which was shown to successfully reproduce gravity-driven segregation according to particle density in rotating drums [11]. Specifically, particles lighter than the surrounding mixture of particles experience a buoyancy force greater than their weight and rise, and particles denser than the surrounding mixture sink. For example, for flow of such a mixture down an plane inclined by θ relative to the horizontal, the segregation flux of the denser particles normal to the flow may be expressed according to:

$$f_d(v_d - v) = K[(\rho_d - \rho_l)/\rho_d] f \phi_d \phi_l. \tag{1}$$

Here $K = CV\rho_d g\cos\theta$ is a characteristic "segregation velocity," where C is inversely related to resistance to local relative motion and V is the volume of a particle. v_i is the velocity component of species i in the segregation direction, typically normal to the system-averaged flow direction. ρ_i is the material density of species i, f_i is the local solids fraction of species i, and ϕ_i is the local concentration of particles of species i ($\phi_i = f_i/\Sigma_i f_i$). The subscripts $i = d$ and l denote denser and less dense particles, respectively. For the variables associated with the mixture dynamics no subscript is used (e.g., $f = f_d + f_l$). We note one potentially confusing issue: While one would expect v, the system-averaged velocity for the segregation direction, to be zero, there are exceptions in some practical applications of this framework. For example, in the flow of particles in a thin surficial layer in a rotating drum (an original application for Eq. (1) in Ref. [10]), the particles dilate as they move through the first half of the flowing layer and then they contract though the second half. Still, the local value for v is typically taken to be the velocity in the *spatially averaged* flow direction rather than the normal direction at each location. To account for cases such as this, for the purposes of the discussion in this paper, we keep the explicit representation in v in Eq. (1) and related expressions of the segregation flux.

More recent work by Khakhar and colleagues (Refs. [13,27,28]) illuminated the form of the inverse drag function C by considering movement of particles differing in density through an *effective* medium and showed the drag increased with an effective temperature. While this latter work demonstrated how temperature should influence the drag coefficient, it did not address the issue of temperature as a driving force of segregation alone. When considering results from mixtures of different-sized particles, one would expect temperature gradients to have the ability to segregate particles in high-f systems as well.

In particular, we recently showed that gradients in granular temperature (or kinetic stress) associated with shear rate gradients can drive segregation in high-f sheared mixtures of different-sized particles [19,29,30]. Further, we showed that at relatively high solids fraction f, the segregation tendency reversed. That is, on the one hand, we found that in sparse systems large particles segregate to regions of low granular temperature and low shear rates, consistent with previous reports (e.g., Refs. [20–23,25]). On the other hand, we found that at higher solids fractions, $f \approx 0.5$ to 0.6, the large particles segregate to regions of high granular temperature. To this point, no analogous study has been performed for mixtures of particles differing only in density. Further, one would expect the segregating effects of granular temperature gradients should compete with the "buoyancy effect" in these mixtures, an important detail for predicting and possibly manipulating segregation in high-f sheared flows.

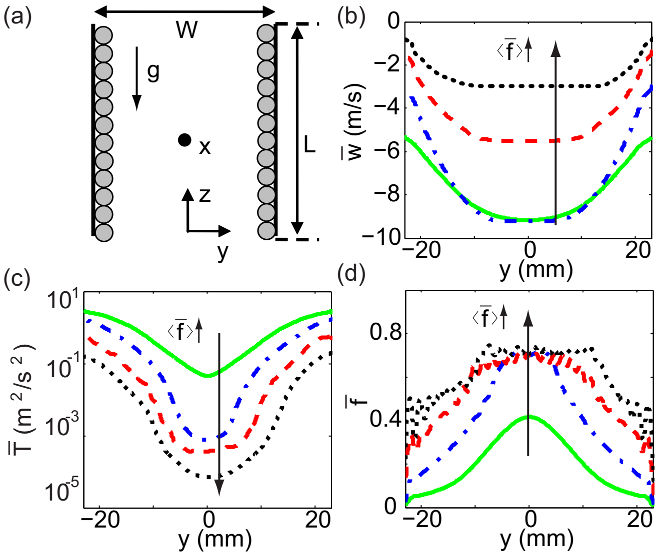

FIG. 1. (Color online) (a) Sketch of a vertical chute. [(b)–(d)] Time-averaged profiles of kinematic quantities for four mixtures at steady state, here $t =$ 5–6 s for $\langle f \rangle = 0.2$ (green solid curve), $t =$ 20–30 s for $\langle f \rangle = 0.4$ (blue dash-dotted curve), $t =$ 30–40 s for $\langle f \rangle = 0.5$ (red dashed curve), and $t =$ 300–310 s for $\langle f \rangle = 0.6$ (black dotted curve): (b) streamwise velocity $\overline{w}$ of the mixture, (c) kinematic granular temperature $\overline{T} = (\overline{u'u'} + \overline{v'v'} + \overline{w'w'})/3$ of the mixture, and (d) local solids fraction of the mixture $\overline{f}$.

In this paper, we describe our computational and theoretical efforts to understand the effects of granular temperature gradients on segregation of binary mixtures differing only in material density, particularly for high solids fractions. To isolate the effect of shear rate gradients from the effect of gravity, we present discrete element method (DEM) simulations of mixtures of particles differing only in density sheared in a vertical chute [Fig. 1(a)]. The vertical chute is ideal for studying the effect of shear rate gradients and associated granular temperature gradients on segregation because of its simple geometry but inhomogeneous flow structure. To determine whether there is a segregation transition analogous to that in mixtures of particles differing only in size, we simulate mixtures over a range of solids fractions, from sparse to high solids fractions. We investigate two theories for their ability to reproduce segregation in these systems: (1) kinetic theory and (2) our mixture theory previously derived for mixtures of different-sized particles [19,29]. We show that kinetic theory is qualitatively effective at all solids fractions we investigate but breaks down quantitatively at high solids fractions. Our mixture theory, focused on effects associated with shear rate gradients, such as gradients in granular temperature and kinetic stress, adapts reasonably well to these mixtures of particles differing only in density. In present form, though, our theory lacks quantitative detail. In our discussion and conclusion sections, we point out shortcomings of this new model and describe ongoing work to improve upon the details.

II. SIMULATION METHOD AND SETUP

For our computational simulations, we use the DEM [31] with a soft sphere model so that each interparticle contact typically endures over several time steps. As is typical, we calculate the forces on each particle at each time step, and from these deduce the subsequent movements and positions of all particles throughout the simulations. We use a nonlinear interparticle contact model based on Hertzian and Mindlin contact theories [32] with damping components calculated based on experimental data (Ref. [33]). The interparticle forces $\boldsymbol{F} = \boldsymbol{F}_n + \boldsymbol{F}_t$; each has components normal ($\boldsymbol{F}_n$) and tangential ($\boldsymbol{F}_t$) to the plane of contact:

$$F_n = -k_n \delta_n^{3/2} - \eta_n \delta_n^{1/4} \dot{\delta}_n, \tag{2a}$$

$$F_t = \min\{-k_t \delta_n^{1/2} \delta_t - \eta_t \delta_n^{1/4} \dot{\delta}_t,\ \mu F_n\}, \tag{2b}$$

In these equations, δ_n and δ_t denote deformations from interparticle contact as effective overlap in the directions normal and tangential to the plane of contact; throughout these equations, subscripts n and t refer to the directions normal and tangential to the plane of contact, respectively. $\boldsymbol{V}_n = (d\delta_n/dt)\boldsymbol{n}$ and $\boldsymbol{V}_t = (d\delta_t/dt)\boldsymbol{t}$ are relative velocities of contacting particles. $\boldsymbol{n}$ and $\boldsymbol{t}$ are unit vectors in each direction. k_n, k_t, η_n, and η_t are interaction coefficients derived from material properties as described in Refs. [32] and [33]. Sliding occurs according to the Coulomb law of friction when $|\boldsymbol{F}_t|/|\boldsymbol{F}_n|$ exceeds the coefficient of friction μ. The material properties to calculate the interaction coefficients are based on particles 2 mm in diameter with all properties similar to "glass" particles, except material density: one particle density is similar to that of glass and the other to that of steel (Table I). The interaction coefficients for all contacts in the mixtures we describe in this paper are shown in Table II. For the simulations described here, we use an equal volume of the two types of spheres. Each species has a 10% polydispersity in the particle diameters to impede particle ordering.

The boundary conditions for our simulations are those of a vertical chute of dimensions $D = 20$ mm, $W = 50$ mm, and $L = 50$ mm in the x, y, and z directions, respectively [Fig. 1(a)]. Our chute has one pair of vertical side walls (perpendicular to the y direction), which are roughened using 2-mm spheres in a random close-packed arrangement. The boundaries are periodic in the z (vertical) and x directions. We perform simulations for several different total system-averaged solids fractions from $\langle f \rangle = 0.2$ to 0.6 by varying the total numbers of particles in the systems (from ≈2500 to 8000 particles). We denote the velocity $\boldsymbol{u} = u\boldsymbol{x} + v\boldsymbol{y} + w\boldsymbol{z}$ according to the directions noted in Fig. 1(a).

TABLE I. Material properties used in DEM simulations. The less-dense particles have similar properties to glass, although to reduce the computational time we reduce the Young's modulus by a factor of O(10^2), similarly to our previous studies [29,30]. The denser particles have the same properties except density, which is close to that of steel.

Property	Less dense	Dense
Material density (kg/m^3)	2520	7800
Young's modulus (GPa)	0.1	0.1
Poisson ratio	0.22	0.22

TABLE II. Values of contact parameters used in the force model for the DEM simulations for the three possible pairs of interacting particles, as indicated in the first row.

Parameters	Less dense	Denser	Less dense Denser
k_n (N/m$^{3/2}$)	1.57×10^6	1.57×10^6	1.57×10^6
k_t (N/m$^{3/2}$)	2.06×10^6	2.06×10^6	2.06×10^6
η_n (N s/m$^{5/4}$)	2.85×10^{-1}	5.01×10^{-1}	3.50×10^{-1}
η_t (N s/m$^{5/4}$)	3.26×10^{-1}	5.74×10^{-1}	4.01×10^{-1}
μ	0.4	0.4	0.4

For each simulation, the particles are initially arranged randomly in the chute and then released with small random velocities. After their initial release, particles collide with one another and with the vertical walls. Dissipation of energy through interparticle and wall-particle interactions limits the velocity throughout the cell, and a steady-state velocity is reached for most of the simulations after a time between a fraction of a second and several seconds, as will be discussed. Exceptions will be noted below. We monitor the segregation and other kinematics until the segregation appears to have reached steady state and then terminate the simulations (as discussed in Sec. III).

III. SIMULATION RESULTS

The steady-state profiles of the streamwise velocity $\overline{w}$, the sum of the mean-square velocity fluctuations (what one might call the kinematic granular temperature $\overline{T} = (\overline{u'u'} + \overline{v'v'} + \overline{w'w'})/3$), and the solids fraction $\overline{f}$ for the mixture are plotted in Figs. 1(b)–1(d). (Here and throughout we use the notation $\overline{q}$ to denote the time average of measured quantity q. We average over the results over relatively short times in the segregation process, typically 0.5-s intervals.) We note these results are similar to those previously published for mono-disperse systems (e.g., Refs. [34–36]) and for mixtures of particles differing only in size (Refs. [19,26,29]). At high $\langle f \rangle$, the velocity profile $\overline{w}(y)$ resembles a plug flow with high shear rates at the side walls, while at the lower solids fractions, the velocity is higher and the profile is roughly parabolic [Fig. 1(b)]. In all cases, $\overline{T}$ is highest near the walls where the shear rate $\dot{\gamma} = |d\overline{w}/dy|$ is the greatest and increases at every point as $\langle f \rangle$ decreases [Fig. 1(c)]. Regions of high $\overline{T}$ and high $\dot{\gamma}$ (near the walls) correspond to regions of low $\overline{f}$ [Fig. 1(d)].

Figure 2 shows snapshots at the beginning and the end of the simulations for three representative solids fractions ($\langle f \rangle = 0.2, 0.4$, and 0.6). Segregation occurs in the horizontal direction

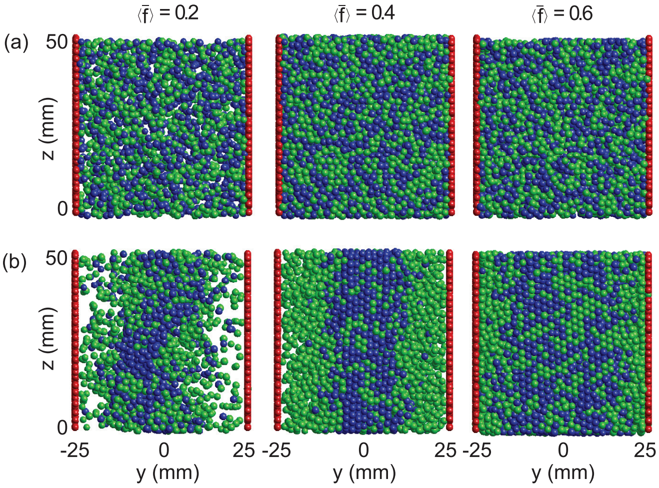

FIG. 2. (Color online) Snapshots of three mixtures at the beginning and steady state of each simulation. (The steady-state time is determined using data plotted in Fig. 4.) (a) The beginning of the simulations ($t = 0$ s). From left to right, $\langle f \rangle = 0.2$, 0.4, and 0.6, respectively; (b) the steady state of the simulations. From left to right, $\langle f \rangle = 0.2$ at $t = 5$ s, $\langle f \rangle = 0.4$ at $t = 10$ s, and $\langle f \rangle = 0.6$ at $t = 300$ s, respectively. The different species are distinguishable by color: 2-mm denser particles, blue (dark); 2-mm less-dense particles, green (light).

under gradients of shear rate and granular temperature for all three $\langle f \rangle$'s. In all cases, all of the particles show some tendency to concentrate to regions of low $\overline{T}$, low $\dot{\gamma}$, and high $\overline{f}$ in the center of the chute, though the denser particles do so more effectively. In contrast with our results for different-sized particles [26], there is no segregation transition, or reversal, at intermediate solids fractions for different-density particles. This distinction may point toward an important difference in the segregation drivers of each at higher system solids fractions. We comment on this more in the conclusion section.

Additionally, we note that the degree of segregation in the steady-state segregation patterns appears most pronounced for the intermediate value of $\langle f \rangle$; in other words, qualitatively, the particles appear less segregated at the smallest and highest system solids fractions. This was also not observed in the case of mixtures of different-sized particles, where, in the steady-state segregation pattern, the segregation appeared equally well pronounced for the mixtures of different-sized particles for all solids fractions ($\langle f \rangle = 0.2$ to 0.6) we investigated.

The profiles of the solids fraction and segregation fluxes for each component in Fig. 3 support the qualitative observations. We plot the solids fraction profiles $\overline{f}_i$ of each component i ($i = d$ for denser particles and $i = l$ for less dense particles) and for the mixture $\overline{f}$ at the steady state $\langle f \rangle = 0.2$, 0.4, and 0.6 in Fig. 3, row 1. The data for $\overline{f}$ clearly show the result of the migration of all particles to the center of the chute. At the larger values of $\langle f \rangle$ (e.g., 0.4 or 0.6), the maximum local solids fraction of mixture is as high as 0.71, close to hexagonal close packing. The relative segregation of the particles at steady state is also apparent in these plots. In all cases, the denser particles have a higher solids fraction in the middle region of the chute than the less-dense particles; this is most pronounced for $\langle f \rangle = 0.4$, supporting our observations that segregation seemed most pronounced in the snapshots from $\langle f \rangle = 0.4$ in Fig. 2.

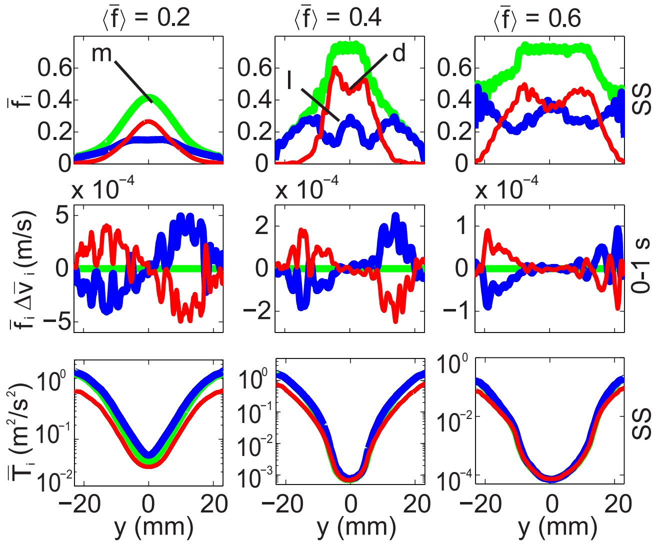

FIG. 3. (Color online) Segregation kinematics of three systems with $\langle f \rangle$ as noted on top of each column for the mixture (m) [green (lighter line)] and dense (d) [red (darker line)] and less dense (l) [blue (bold dark line)] particles. Row 1: $\overline{f}_i$ at steady state (SS). Row 2: Segregation fluxes $\overline{f}_i \Delta \overline{v}_i$ as defined in text averaged over $t = 0 - 1$ s (row 2). Row 3: Kinematic granular temperature $T_i = (\overline{u_i' u_i'} + \overline{v_i' v_i'} + \overline{w_i' w_i'})/3$ at steady state. We note that the scales of the vertical axes in rows 2 and 3 vary for the different solids fractions.

Row 2 of Fig. 3 shows the profiles of the horizontal segregation fluxes $\overline{f}_i \Delta \overline{v}_i = \overline{f}_i (\overline{v}_i - \overline{v})$ at the beginning of the simulations for these systems. For all three $\langle f \rangle$'s, the horizontal fluxes are strong and clear: the denser particles have positive fluxes in the left half of the chute and negative fluxes in the right half of the chute, indicating denser particles segregate to the center of the cell, while the less dense particles segregate to the walls. The relative segregation fluxes decrease for higher values of $\langle f \rangle$, which is possibly due to a decrease of gradients of $\dot{\gamma}$ and $\overline{T}$ as $\langle f \rangle$ increases [see Figs. 1(b) and 1(c)].

Row 3 of Fig. 3 shows the profiles of $\overline{T}$ which we include because of its demonstrated importance in driving segregation in certain systems (e.g., Refs. [20,21,29]). In the sparse flow, the less-dense particles have a higher value of $\overline{T}$ than denser particles, which one might expect when considering momentum exchange among particles of different density (e.g., Ref. [37]). On the other hand, in the system of highest solids fraction ($\langle f \rangle = 0.6$), the difference between species kinematic temperatures is minimal, especially at the center of the chute cell. This is consistent with our previous observations of highly concentrated mixtures in a drum [37], where we argued that in high solids fraction sheared flows, the velocity fluctuations did not differ for particles of similar size, regardless of their relative density because of geometric considerations of the particle movements.

We consider two quantities to determine the temporal evolutions of the mixture dynamics. The first is the width-averaged vertical velocity of the particles in the chute $\langle w \rangle$. We used this to estimate the time dependence of the average

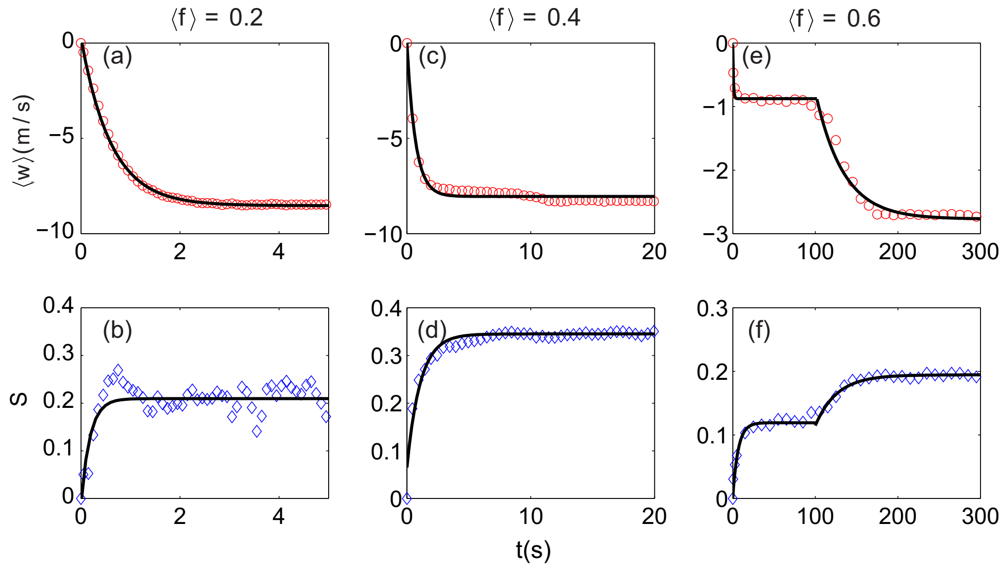

FIG. 4. (Color online) Time dependence of average downstream velocity $\langle w\rangle$ and segregation index S: First row shows plots of the downstream velocity averaged across the width of the chute $\langle w\rangle = \sum_{j=0}^{N_{\rm bin}} \overline{f}_j \overline{w}_j / \sum_{j=0}^{N_{\rm bin}} \overline{f}_j$, where $\overline{w}_j$ and $\overline{f}_j$ are the average vertical velocity and average solids fraction of the mixture in bin j and $N_{\rm bin} = 2500$ is the number of bins in the y direction and the second row shows plots of a measure of the segregation in the chute S [see Eq. (3)]. Symbols are data measured from DEM simulations and solid lines are exponential fits to the data. For $\langle f\rangle = 0.2$ and 0.4, the fit equations are $f(t) = A + B\exp(-t/\tau)$. For $\langle f\rangle = 0.6$, when $t < 100$ s (stage I), the fit equation is the same as those at $\langle f\rangle = 0.2$ and 0.4, and when $t > 100$ s (stage II), the fit equation is $f(t) = A + B\exp[-(t - t_0)/\tau]$. Here A, B, t_0, and τ are fitting parameters: $A + B$ and A represent the initial and final values for each variable, τ is the time scale, and t_0 is indicative of the effective start time of the exponential decay during stage II for $\langle f\rangle = 0.6$. The fitting coefficients are shown in Table III.

kinematics of the mixture. The second measure we used provides a systematic measure of the rate and degree of segregation, S, essentially, the standard deviation of mean concentration S_i of each species i at each time step t:

$$S_i(t) = \sqrt{\sum_{j=1}^{N_{\rm bin}} \{[\phi_i(t)]_j - \langle\phi_i\rangle\}^2/(N_{\rm bin} - 1)}. \tag{3}$$

Here $N_{\rm bin} = 2500$ is the number of bins in the y direction, $[\phi_i(t)]_j = (f_i/f)_j$ is the mixture concentration of species i in bin j at time t, and $\langle\phi_i\rangle = \langle f_i\rangle/\langle f\rangle$ is mean (volume) concentration of this species in the system (0.5 for both species). Since $\langle\phi_d\rangle = \langle\phi_l\rangle = 0.5$ and $[\phi_d(t)]_j + [\phi_l(t)]_j = 1$ (for all t), $S_d = S_l$, which we denote by S.

Figure 4 shows the time dependence of $\langle w\rangle$ [Figs. 4(a), 4(c), and 4(e)] and S [Figs. 4(b), 4(d), and 4(f)] for the same three systems presented in Figs. 2 and 3. For a sense of the spatial resolution of the evolving segregation patterns in these systems, we plot the spatiotemporal profiles of the concentration of the denser particles in Figs. 5(a)–5(d). In all systems at early times, $\langle w\rangle$ and S grow asymptotically from 0 to constant values, at which point the mean flow kinematics and segregation reach a steady state. For $\langle f\rangle = 0.6$, this growth takes place in two stages: first, $\langle w\rangle$ and S increase to relatively constant values within a few seconds and remain essentially steady until $t \approx 100$ s [see Fig. 4(e)], and then the particles suddenly accelerate again and segregate further until another set of relatively constant values for $\langle w\rangle$ and S is reached; $\langle w\rangle$ and S remain steady once again until we stop the simulation at $t \approx 300$ s [Fig. 4(e)]. The time of this transition from one apparent metastable state to the next differs with different initial conditions. We see evidence for a similar transition for our moderate density system [$t \approx 10$ s in Fig. 4(c)], though the effect on segregation rate, if any, is negligible [Fig. 4(d)]. The reacceleration of the flow is possibly due to a relatively minor but sudden rearrangement of particles in the near-close-packed

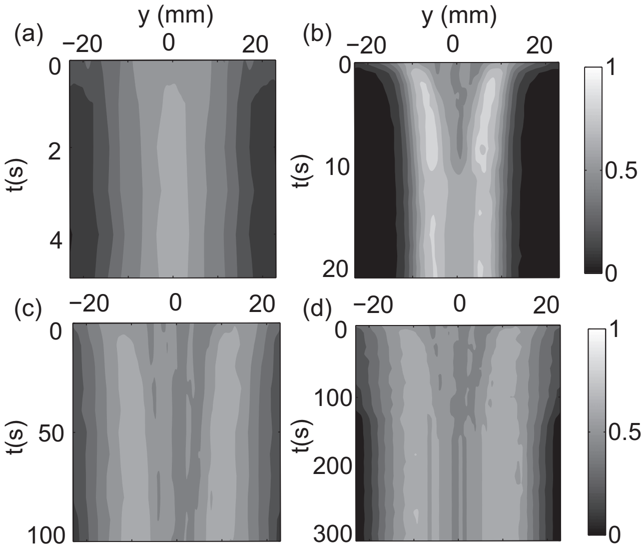

FIG. 5. Spatiotemporal profiles of concentration of denser particles ($\phi_d = f_d/f$) for (a) $\langle f\rangle = 0.2$ at $t = 0$–5 s, (b) $\langle f\rangle = 0.4$ at $t = 0$–20 s, (c) $\langle f\rangle = 0.6$ at $t = 0$–100 s, and (d) $\langle f\rangle = 0.6$ at $t = 0$–300 s. The legend indicates the shade of gray that corresponds to particular fraction of denser particles. For example, $\phi_d = 1$ for white pixels and $\phi_d = 0$ for black pixels.

TABLE III. Values of fitting coefficients for $\langle w\rangle$ and S.

	A_w (m/s)	B_w (m/s)	τ_w (s)	$t_{0,w}$ (s)	A_S	B_S	τ_S (s)	$t_{0,S}$ (s)
$\langle f\rangle = 0.2$	−8.53	8.83	0.61	–	0.21	−0.22	0.18	–
$\langle f\rangle = 0.4$	−8.05	8.05	0.69	–	0.35	−0.28	1.08	–
$\langle f\rangle = 0.6$(I)[a]	−0.88	0.85	0.82	–	0.12	−0.12	6.60	–
$\langle f\rangle = 0.6$(II)[a]	−2.77	2.00	33.90	101	0.19	−0.077	26.22	100

[a] I and II represent two stages of the flow.

region similar to cage-breaking in similarly dense sheared flows [38]. These dynamics could also be related to a jamming transition, a matter that is currently under investigation.

To compare the rate for each system to reach steady state and the segregation rate at different systems, we fit the curves of $\langle w\rangle$ and S in Fig. 4 using one of two exponential relations:

$$f(t) = A + B\exp(-t/\tau), \tag{4a}$$

$$g(t) = A + B\exp[-(t - t_0)/\tau], \tag{4b}$$

where fitting parameters A and B are the fitted initial $(A + B)$ and final (A) values for each variable, and τ is the time scale of each process. We fit the data from $\langle f\rangle = 0.2$ and 0.4 using Eq. (4a). During the first stage of $\langle f\rangle = 0.6$, we fit the variables using Eq. (4a), and during the second stage (from $t = 100$ to 300 s, determined empirically) we use Eq. (4b), where $t = 100$ s is our empirically determined start time for the second stage of the system evolution.

The values of these fitting parameters for $\langle w\rangle$ and S for the three different $\langle f\rangle$'s are listed in Table III. The time scale for both $\langle w\rangle$ and S (τ_w and τ_S, respectively) increase as $\langle f\rangle$ increases, though the increase of τ_w is not as pronounced as for τ_S. The average flow in the sparsest system ($\langle f\rangle = 0.2$), takes longer for the mean flow to reach the steady state than the essential segregation ($\tau_w > \tau_S$). When $\langle f\rangle$ increases to 0.4, τ_w is comparable to τ_S. For $\langle f\rangle = 0.6$, τ_S is 8 times larger than τ_w in stage I, indicating segregation of the two species is still evolving when the mean flow has reached steady state.

As mentioned, segregation in the sparse system has been previously shown to be driven by the gradients of granular temperature, which can be modeled by the kinetic theory [21,25]. We have shown that segregation can also be driven by gradients in shear rate and granular temperature gradients [26]. In Sec. IV A, we use a kinetic theory approach to model the shear-induced density segregation in the vertical chute. The kinetic theory captures the segregation trends and fluxes at sparse systems (e.g., $\langle f\rangle = 0.2$), but it overestimates the segregation fluxes when the system concentration increases ($\langle f\rangle \geqslant 0.4$). Next, we adapt a recently developed theory [29] based on a mixture theory to understand the driving mechanisms for shear-induced density segregation for the higher $\langle f\rangle$ systems.

IV. TWO MODELS FOR SHEAR-INDUCED SEGREGATION

We consider these results in the context of two models. The first is kinetic theory for binary mixtures of slightly inelastic particles as detailed in Ref. [23]. The second is based on a model we previously proposed for different-sized, same-density particles, described in detail in Refs. [19,29].

A. Kinetic theory adapted for the vertical chute problem

To compare our simulation results with those predicted by kinetic theory, we consider that our particles are slightly dissipative (restitution coefficient $e \approx 0.9$) and that what we might call the dynamic temperature of each species [the kinetic energy of the velocity fluctuations, $T_D = m_i T_i$ typically differ from one another (m_i is the particle mass of species i)]. As in Ref. [30], we use expressions derived under the framework of kinetic theory assuming a Maxwellian velocity distribution and allowing the particles to be slightly inelastic and that includes the effect of nonequipartition of temperature [37,39,40] according to expressions in Ref. [23] (similar to those in Ref. [20]).

To compare predictions from kinetic theory with our simulation results, we focus on segregation in the y direction (see Fig. 2) within the first 1 s of the simulation. In Fig. 6, we plot the difference in the average "segregation" or "diffusion" velocities $\overline{v}_l - \overline{v}_d$ of the two species from the DEM simulations and as predicted according to expressions developed from kinetic theory. (We note that the details on how the theoretical values are calculated are included in Appendix A.)

In all cases, kinetic theory successfully predicts the segregation trend. Specifically, the dense particles segregate toward the center, and the less-dense particles segregate toward the walls. For the sparse system ($\langle f\rangle = 0.2$), kinetic theory successfully predicts the relative segregation velocities both qualitatively and quantitatively. The predicted fluxes are slightly larger than those measured from the simulation. This is probably due to the existence of "density waves" of locally high concentrations of particles as reported by Liss *et al.* [41] in this system [apparent in Fig. 2(b)], which is not accounted for in the development of the predictions we report here from kinetic theory (Appendix A). However, when the system is more concentrated ($\langle f\rangle \geqslant 0.4$), kinetic theory overpredicts the relative segregation velocities. At $\langle f\rangle = 0.6$, the predicted segregation fluxes are one order of magnitude larger than fluxes from the simulation. These results indicate that kinetic theory can qualitatively predict segregation fluxes in agreement with previous work [21,25]. However, as the system becomes more concentrated ($\langle f\rangle \geqslant 0.4$), kinetic theory overestimates segregation fluxes as also found by Xu *et al.* [25], and the difference between theory and results increases as $\langle f\rangle$ increases.

B. Mixture theory with "temperature effects" adapted to density variations

We next consider a model we developed to account for the effect of temperature gradients on segregation in sheared

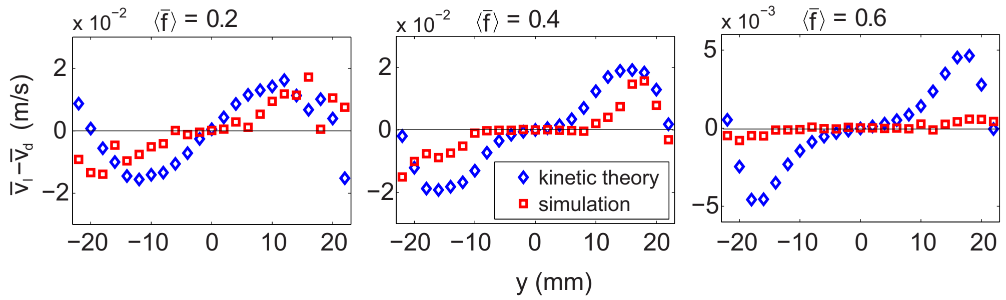

FIG. 6. (Color online) Profiles of the relative diffusion velocities $\overline{v}_l - \overline{v}_d$ between less dense and denser particles in the y direction averaged across the width of the chute and over the first 1 s for three different systems with $\langle f \rangle$ indicated in the figure. Solid lines denote $\overline{v}_l - \overline{v}_d = 0$ to guide eye.

high-$\langle f \rangle$ systems for particles differing only in size to determine whether it can be adapted to model the segregation effects we see here for mixtures of particles differing in material density. Our mixture theory model is more simplistic than kinetic theory in that it does not start at the particle scale to develop rules for interactions between species. Rather, the interaction forces are based on some macroscopic assumptions of the mechanics of the interactions. In that way, this theory is more easily adaptable to different boundary conditions, but one must use caution in interpreting the results.

The basic form of the model is described in detail in Refs. [19,29], adapted to gravity-driven flow in Ref. [42]. The model development in our earlier work was based, in part, on the assumption that the solids fraction f is uniform throughout for equal-density particles, and, therefore, so is what we might call the mixture *bulk density* defined by $\rho = f\rho_m$. For segregating mixtures of particles differing in material density, even if f is uniform, ρ becomes nonuniform as the mixture segregates. In this section, we outline our theory following much of the development we described in Refs. [19,29] but modified to allow for a spatially varying particle density and then compare it with our DEM results.

1. Overview of mixture theory

As in the description for the DEM results, we denote bulk Eulerian properties of each species with subscripts and those of the mixture of both species together as variables without subscript (e.g., $\rho = \Sigma_i \rho_i$ and $\rho_i = \rho_{m,i} f_i$). We first consider conservation of mass and momentum for the mixture:

$$\frac{\partial \rho}{\partial t} + \nabla \cdot (\rho \boldsymbol{u}) = 0, \tag{5a}$$

$$\frac{\partial}{\partial t}(\rho \boldsymbol{u}) + \nabla \cdot (\rho \boldsymbol{u} \otimes \boldsymbol{u}) = \nabla \cdot \sigma + \boldsymbol{F}, \tag{5b}$$

and the same for the individual species:

$$\frac{\partial \rho_i}{\partial t} + \nabla \cdot (\rho_i \boldsymbol{u}_i) = 0, \tag{6a}$$

$$\frac{\partial (\rho_i \boldsymbol{u}_i)}{\partial t} + \nabla \cdot (\rho_i \boldsymbol{u}_i \otimes \boldsymbol{u}_i) = \nabla \cdot (\boldsymbol{\sigma}_i) + \boldsymbol{F}_i + \boldsymbol{\beta}_i. \tag{6b}$$

In these equations, $\boldsymbol{\sigma}$ is the stress tensor using the relatively standard sign convention for stresses as, for example, noted in Ref. [43], and $\boldsymbol{F}$ represents the net body force per unit volume. $\boldsymbol{\sigma}_i$ is the local stress borne by species i, and the total stress $\boldsymbol{\sigma} = \sum \boldsymbol{\sigma}_i$. $\boldsymbol{\beta}_i$ represents the interaction force exerted on species i by the other species.

We then consider the instantaneous value of each variable q at position $\boldsymbol{r}$ as a sum of the local temporal average $\overline{q}(\boldsymbol{r})$ and the difference between its instantaneous value and the average $q'(\boldsymbol{r},t) = q(\boldsymbol{r},t) - \overline{q}(\boldsymbol{r})$ (typically called "Reynolds decomposition" [44]). We consider the results in the context of pseudo-two-dimensional systems like the vertical chute so the flow exhibits uniformity in the directions perpendicular to segregation (e.g., x and z directions). We rewrite the momentum equation (5b) for the mixture in the y direction as

$$\frac{\partial}{\partial t}(\overline{\rho} + \rho')(\overline{v} + v') + \frac{\partial}{\partial y}[(\overline{\rho} + \rho')(\overline{v} + v')(\overline{v} + v')] = \frac{\partial}{\partial y}(\overline{\sigma}_{yy} + \sigma'_{yy}) + \overline{F}_y + F'_y. \tag{7}$$

We consider systems in which the mixture velocity reaches steady state (as in the majority of the segregation for $\langle f \rangle = 0.6$ in Fig. 4, row 3). We approximate the correlations between velocity fluctuations and concentrations as negligible (as we found in Ref. [29]). Finally, for this paper, we restrict our discussions to cases where the only body force (particle weight) is in the z direction, like the vertical chute. Then the Reynolds averaged equations in the y direction may be expressed as:

$$\frac{\partial \overline{\sigma}^{\boldsymbol{c}}_{yy}}{\partial y} + \frac{\partial \overline{\sigma}^{\boldsymbol{k}}_{yy}}{\partial y} = 0, \tag{8}$$

for the mixture and

$$\frac{\partial \overline{\sigma}^{\boldsymbol{c}}_{yy,i}}{\partial y} + \frac{\partial \overline{\sigma}^{\boldsymbol{k}}_{yy,i}}{\partial y} - \overline{\beta}_{y,i} = 0 \tag{9}$$

for the individual components. As in Ref. [29], we refer to $\overline{\sigma}^{\boldsymbol{k}}_{yy} \equiv \rho\overline{v'v'}$ as a component of the kinetic stress and define a contact stress tensor $\boldsymbol{\sigma}^{\boldsymbol{c}} = -\boldsymbol{\sigma}$ so terms such as $\overline{\sigma}^{\boldsymbol{c}}_{yy}$ are positive for our problem where there are only compressive, not tensile, interactions between particles. We note that $\rho\overline{v'v'}$ scales roughly with T, so Eq. (8) indicates that a gradient in T can be associated with a gradient in both $\overline{\sigma}^{\boldsymbol{k}}_{yy}$ and $\overline{\sigma}^{\boldsymbol{c}}_{yy}$ (of opposite signs). Since all terms in Eqs. (8) and (9) are averaged, we drop the overbar from this point in this paper, so, unless noted for each variable, q alone refers to the average quantity $\overline{q}$.

In contrast with classic mixture theory (e.g., Refs. [45–47]), we follow Refs. [29,42] and references within and allow the partitioning of kinetic and contact stresses between the species to vary from the associated solids fractions ($\sigma^{\boldsymbol{c}}_{yy,i} \neq \phi_i\sigma^{\boldsymbol{c}}_{yy}$ and $\sigma^{\boldsymbol{k}}_{yy,i} \neq \phi_i\sigma^{\boldsymbol{k}}_{yy}$). Instead, we use independent stress partition coefficients ($\psi^{\boldsymbol{c}}_i$ and $\psi^{\boldsymbol{k}}_i$):

$$\sigma^{\boldsymbol{c}}_{yy,i} = \psi^{\boldsymbol{c}}_i\sigma^{\boldsymbol{c}}_{yy}, \quad \text{and} \quad \sigma^{\boldsymbol{k}}_{yy,i} = \psi^{\boldsymbol{k}}_i\sigma^{\boldsymbol{k}}_{yy}, \tag{10}$$

where $\psi^{\boldsymbol{c}}_i$ and $\psi^{\boldsymbol{k}}_i$ determine the proportion of normal contact and kinetic stresses carried by species i and are not necessarily equal to ϕ_i.

For the interaction term $\beta_{y,i}$, we propose a similar form to that for equal-density particles in Ref. [29], modified slightly to account for the variable species concentrations throughout the system:

$$\beta_{y,i} = \sigma^{\boldsymbol{c}}_{yy}\frac{\partial}{\partial y}\psi^{\boldsymbol{c}}_i + \sigma^{\boldsymbol{k}}_{yy}\frac{\partial}{\partial y}\psi^{\boldsymbol{k}}_i - \rho_i c_D(v_i - v) - d\frac{\partial\rho_i}{\partial y}. \tag{11}$$

The first two terms on the right-hand side of the equation ensure that, as in Darcy's law, the segregation process is driven by intrinsic rather than partial stress gradients (as in Refs. [47–49]). The third term is a linear drag law, and c_D is a linear drag coefficient. The fourth term acts as a "remixing force" that drives grains of constituent i towards areas of lower concentration, and d is an ordinary diffusion coefficient.

Combining Eqs. (10) and (11) with Eq. (8), a segregation flux of species i can be expressed as:

$$\rho_i(v_i - v) = \frac{\left(R^{\boldsymbol{c}}_i - R^{\boldsymbol{k}}_i\right)\phi_i}{c_D}\frac{\partial\sigma^{\boldsymbol{k}}_{yy}}{\partial y} - \frac{d}{c_D}\frac{\partial\rho_i}{\partial y}. \tag{12}$$

$R^{\boldsymbol{c}}_i = \psi^{\boldsymbol{c}}_i/\phi_i$ and $R^{\boldsymbol{k}}_i = \psi^{\boldsymbol{k}}_i/\phi_i$ are stress partition variables we introduce to facilitate a physical interpretation of the governing features of this equation. Equation (12) is similar to, but more general than, the equivalent expression for equal density particles presented as Eq. (11) in Ref. [29] as:

$$\phi_i(v_i - v) = \frac{\left(R^{\boldsymbol{c}}_i - R^{\boldsymbol{k}}_i\right)\phi_i}{\rho c_D}\frac{\partial\sigma^{\boldsymbol{k}}_{yy}}{\partial y} - \frac{d}{c_D}\frac{\partial\phi_i}{\partial y}. \tag{13}$$

For mixtures of particles of the same material density, ρ can be expressed by $\rho = \rho_m f$, where ρ_m is the material density of *all* species in the mixture, so the two expressions for flux are interchangeable. For our mixtures of particles of different densities $\rho = \rho_{m,d} f_d + \rho_{m,l} f_l$, and the two expressions for flux are not equal.

Otherwise, the predictions are similar. Both Eqs. (12) and (13) predict that if $R^{\boldsymbol{c}}_i = R^{\boldsymbol{k}}_i$, the species will not segregate. However, if $R^{\boldsymbol{c}}_i \neq R^{\boldsymbol{k}}_i$ and $\partial\sigma^{\boldsymbol{k}}_{yy}/\partial y \neq 0$, whichever species carries a higher fraction of the contact stress than they do the kinetic stress should be pushed to the region of higher temperature.

2. *Mixture theory compared with simulation results*

To compare the theoretical predictions with the computational results, we consider that, for the theoretical development, we have assumed that the velocities in the system reach steady state before the majority of the segregation process takes place. This condition is met for the initial segregation that occurs for the highest, $\langle f\rangle \sim 0.6$, so we focus our comparison on this case. We do not have a predictive form for stresses or the coefficients of drag and diffusion. In lieu of a direct comparison of theory and simulation, we investigate the relationships between the segregation flux and partition coefficients measured in the simulations and compare them with those predicted by Eq. (12) to determine whether the theoretical framework is consistent with the simulations. Then we use these data to obtain estimates for the coefficients of drag and diffusion as described shortly.

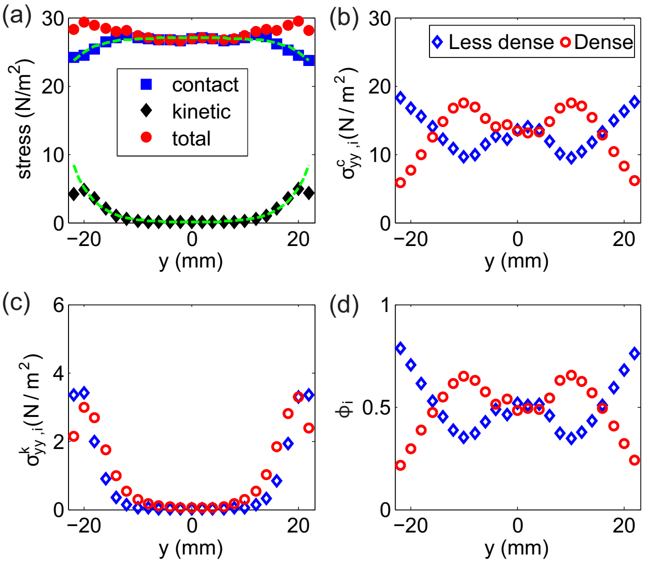

FIG. 7. (Color online) The y component of total and partial normal stresses in the y direction for the mixture and the two species at a quasi steady state ($t = 50$–100 s). (a) Total, kinetic, and contact stresses for the mixture; (b) contact stresses for the two species; (c) kinetic stresses for the two species; (d) species concentrations. The dashed lines in (a) are exponential fits for the kinetic and contact stresses of the mixtures. For kinetic stresses: $\sigma^{\boldsymbol{k}}_{yy}(y) = A\exp(|By|)$ based on a linearized least-squares fit, where $A = 3.6 \times 10^{-2}$ N/m^2 and $B = 0.25$ mm^{-1}; for contact stresses: $\sigma^{\boldsymbol{c}}_{yy}(y) = C - A\exp(|By|)$, where $A = 1.6 \times 10^{-2}$ N/m^2, $B = 0.24$ mm^{-1}, and $C = 27.05$ N/m^2.

We first calculate the stresses and other dynamics in the simulations throughout the system, including the partition coefficients for the partial stresses and the concentration profiles. For the stresses, we follow the same procedure described in Ref. [29], which we summarize in Appendix B. We have found that the stresses do not change considerably over the course of the simulation and plot the profiles from the data averaged over $t = 50$–100 s in the simulation after the mixture kinematics first reach a quasi steady state. In Fig. 7(a), we plot the profiles of $\sigma^{\boldsymbol{k}}_{yy}(y)$ and $\sigma^{\boldsymbol{c}}_{yy}(y)$, which in many ways are similar to those using equal-density, different-sized particle mixtures in Ref. [29]. The profile of $\sigma^{\boldsymbol{k}}_{yy}(y)$ peaks near the rough walls and dips in the middle. As one would expect from Eq. (8), $\sigma^{\boldsymbol{c}}_{yy}(y)$ follows the opposite trend: It is highest in the middle and dips near the walls. The total stress $\sigma^{\boldsymbol{c}}_{yy}(y) + \sigma^{\boldsymbol{c}}_{yy}(y)$ is nearly constant across the chute cell. We fit the data by exponential functions: $\sigma^{\boldsymbol{k}}_{yy}(y) = A\exp(B|y|)$ and $\sigma^{\boldsymbol{c}}_{yy}(y) = C - A\exp(B|y|)$, where the fitting parameters are

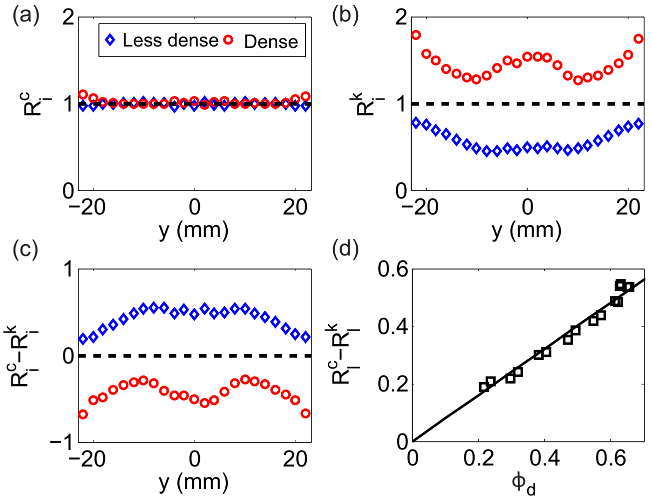

FIG. 8. (Color online) Profiles of partial stress coefficients $R_i^{\boldsymbol{c}}$ (a) and $R_i^{\boldsymbol{k}}$ (b) averaged at $t = 50$–100 s. (c) Profiles of $R_i^{\boldsymbol{c}} - R_i^{\boldsymbol{k}}$. (d) A parametric plot from the data shown in (c) and Fig. 7(d) for $R_L^{\boldsymbol{c}} - R_L^{\boldsymbol{k}}$ vs ϕ_D. The dashed lines in (a)–(c) are used to indicate the case where $R_i^{\boldsymbol{k},c} = 1$ for both components, i.e., indicating the values on the plot for which the stresses would be equally partitioned between the components. The solid line in (d) is a linear least-squared fit for $R_L^{\boldsymbol{c}} - R_L^{\boldsymbol{k}} = B\phi_D$; $B \approx 0.8$.

given in the caption of Fig. 7. Figures 7(b) and 7(c) show the contact and kinetic stresses associated with each of the two species, and Fig. 7(d) shows the concentration profiles of each constituent in the y direction. These results indicate that, depending on the region of the chute, either the less dense or the denser particles may take up a higher fraction of the local stress, and $\sigma^{\boldsymbol{c}}_{yy,i}(y)$ scales most closely with $\phi_i(y)$.

In Fig. 8 we plot the relative partial stress coefficients $R_i^{\boldsymbol{c}} = \psi_i^{\boldsymbol{c}}/\phi_i$ and $R_i^{\boldsymbol{k}} = \psi_i^{\boldsymbol{k}}/\phi_i$, averaged over the time interval $t =$ 50–100 s. $R_i^{\boldsymbol{c}} \approx 1$ except immediately adjacent to the wall, where the results may be affected by the neighboring wall particles. These results indicate that nearly everywhere the contact stress borne by each species is proportional to its local concentration, i.e., $\psi_i^{\boldsymbol{c}} = \phi_i$. In contrast, the denser particles carry a significantly higher fraction of the kinetic stresses than their concentration ($R_d^{\boldsymbol{k}} > 1$, and $\psi_d^{\boldsymbol{k}} > \phi_d$), and the less-dense particles carry a lower fraction of the kinetic stresses than their concentration ($R_l^{\boldsymbol{k}} < 1$, and $\psi_l^{\boldsymbol{k}} < \phi_l$). We briefly note here that these results markedly differ from mixtures of particles differing only in size, where the lighter (smaller) particles carry a higher fraction of the kinetic stress [29,42]. We discuss this more in Secs. V and VI.

The results in the mixtures of particles differing only in density indicate that $R_l^{\boldsymbol{c}} - R_l^{\boldsymbol{k}} > 0$ and $R_d^{\boldsymbol{c}} - R_d^{\boldsymbol{k}} < 0$. Considering this in the context of the theoretical predictions in Eq. (12), the less-dense particles should migrate in the direction of increasing kinetic stress and the denser particles should migrate in the direction of decreasing kinetic stress [Fig. 8(c)]. Since $\partial\sigma^{\boldsymbol{k}}_{yy}/\partial y > 0$ for $y < 0$ and $\partial\sigma^{\boldsymbol{k}}_{yy}/\partial y < 0$ for $y > 0$ [see Fig. 7(a)], Eq. (12) predicts that denser particles segregate to the center of the cell and the less-dense particles segregate to the walls, consistent with our simulation results [e.g., Figs. 2(b) and 3].

We build on these results to develop a prediction for the evolution of the local concentrations of the species. We first consider the equation of conservation of mass for species i. With no gradients in the x and z directions and assuming the solids fraction of the mixture is time independent during segregation ($\partial f/\partial t = 0$), we can rewrite Eq. (6a) as:

$$\rho_{m,i} f \frac{\partial \phi_i}{\partial t} + \frac{\partial}{\partial y}(\rho_i v_i) = 0. \tag{14}$$

We substitute the theoretical form of the segregation flux expressed in Eq. (12) into Eq. (14), and we find:

$$\rho_{m,i} f \frac{\partial \phi_i}{\partial t} + \frac{\partial}{\partial y}\left[\frac{\left(R_i^{\boldsymbol{c}} - R_i^{\boldsymbol{k}}\right)\phi_i}{c_D}\frac{\partial \sigma^{\boldsymbol{k}}_{yy}}{\partial y} - \frac{d}{c_D}\frac{\partial \rho_i}{\partial y}\right] = 0. \tag{15}$$

Comparing the concentration profiles in Fig. 7(d) with profiles of $R_i^{\boldsymbol{c}} - R_i^{\boldsymbol{k}}$ in Fig. 8(c) indicates that the magnitude of $R_i^{\boldsymbol{c}} - R_i^{\boldsymbol{k}}$ for each species is correlated with the concentration of the other species. We plot $R_l^{\boldsymbol{c}} - R_l^{\boldsymbol{k}}$ versus ϕ_d for these data in Fig. 8(d) excluding the creeping regions in the middle of the chute (-6 mm $< y <$ 6 mm). Though not perfectly linear [see fit in Fig. 8(d)], we approximate it as such in Eq. (15), i.e., $R_l^{\boldsymbol{c}} - R_l^{\boldsymbol{k}} \approx B\phi_d$, where B is a fitting parameter. (We determined that $B \approx 0.8$ by fitting the data in Fig. 8.) Then Eq. (15) may be rewritten for the less dense particles as:

$$\frac{\partial \phi_l}{\partial t} + \frac{B}{c_D \rho_{m,l} f}\frac{\partial}{\partial y}\left[\phi_l(1-\phi_l)\frac{\partial \sigma^{\boldsymbol{k}}_{yy}}{\partial y}\right] - \frac{d}{c_D f}\frac{\partial^2 f\phi_l}{\partial y^2} = 0. \tag{16}$$

The spatiotemporal profiles of concentration of less dense particles can then be obtained by solving Eq. (16) numerically, though $f(y)$, $\partial\sigma^{\boldsymbol{k}}_{yy}/\partial y$, diffusivity $D = d/c_D$, and the ratio $q = B/c_D$ (an indication of the segregation magnitude) must be obtained. For $f(y)$ and $\partial\sigma^{\boldsymbol{k}}_{yy}/\partial y$ we use the profiles of the mixture solids fraction [Fig. 1(d)] and normal kinetic stresses in the y direction [Fig. 7(a)] obtained from the simulations. We do not know D and q; for simplicity, we choose constant values for these two parameters empirically by comparing the predictions obtained using different values of D and q to the simulation results. For our numerical solution, we use initial conditions consistent with a homogenous mixture ($\phi_d = \phi_l = 0.5$ at $t = 0$ for all values of y) and no-flux conditions at the two walls [$-q(1-\phi_l)\phi_l(\partial\sigma^{\boldsymbol{k}}_{yy}/\partial y)/\rho_{m,l} = D\partial(f\phi_l)/\partial y$ at $y = \pm 25$ mm for all values of t]. We then discretize the problem and solve numerically by using a central difference scheme for spatial derivatives and modified Euler method for time integration.

Figure 9 shows spatiotemporal profiles of concentration of less dense particles from theoretical predictions up to 300 s. Based on trial and error we chose $q = 1 \times 10^{-3}$ s and $D = 0.2$ mm^2/s. The value for D is similar to that we found for a mixture of 2-mm and 3-mm particles in a drum, where we found $d = 1.26 \times 10^{-5}$ m^2/s^2 and $c_D = 6.3$ s^{-1} so $D \approx 0.2$ mm^2/s. On the other hand $c_D = B/q = 0.8/(10^{-3}$ s$) = 800$ s^{-1} is significantly larger than that for the mixture of different-sized particles ($\approx$6.3 s^{-1}). It is likely that both D and c_D vary with details such as the local shear rate as in Refs. [13,28,50], so such comparisons are not so useful, but rather the next generation of the model should consider a more

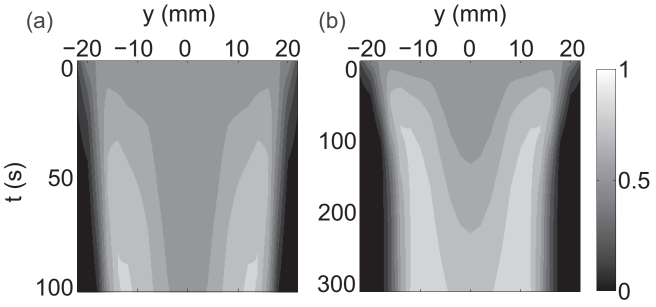

FIG. 9. Theoretical predictions of spatiotemporal profiles of the concentration of dense particles compared to those in Figs. 5(c) and 5(d). (a) $t = 0$–100 s; (b) $t = 0$–300 s. The legend indicates the shade of gray that corresponds to particular fraction of denser particles. For example, $\phi_d = 1$ for white pixels and $\phi_d = 0$ for black pixels.

physically representative form for these parameters, which we discuss in the next section.

In both the theoretical predictions and simulation results [compare Figs. 9(a) and 9(b) with Fig. 5(c) and 5(d), respectively], the less-dense particles segregate to the side walls, and dense particles segregate toward the center. In the middle of the chute, in the slow creeping region where the gradients of normal kinetic stresses is very small, the segregation process is much slower than in other regions. All of these indicate a good qualitative agreement between theoretical predictions and simulation results. On the other hand, the theory does not capture the sudden intensifying of the segregation pattern that begins ≈100 s in the simulations that appears to be correlated with an increase in average velocity. We hypothesize that this sudden change is associated with an increase in packing efficiency and decrease in relative magnitude of collisional damping of the particle motion that is not captured by the theory.

Finally, with the fitted values of q and D from above, we compare the segregation velocity $v_l - v_d$ predicted by Eq. (12) with the simulation results for the first second and at the steady state ($t = 300$–310 s), as shown in Fig. 10. Our theoretical predictions match well with DEM simulations at both stages of simulations, in contrast to the kinetic theory (Fig. 12), which, based on the local kinematics in the DEM simulations, overpredicts the segregation velocity by approximately one order of magnitude compared with that exhibited by the DEM simulations.

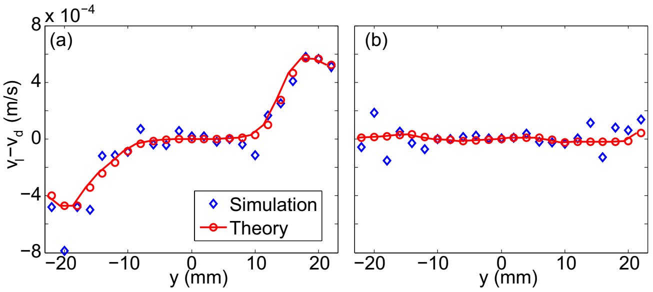

FIG. 10. (Color online) Comparison of profiles of segregation velocity $v_l - v_d$ vs y between theoretical predictions from Eq. (12) and DEM simulations at (a) the first second and (b) $t = 300$–310 s for $\langle f \rangle = 0.6$.

V. DISCUSSION

These results add to the growing body of evidence supporting the importance of velocity fluctuations (via granular temperature and/or kinetic stresses) in driving segregation in high solids fraction granular flows. Effects of velocity fluctuations are typically discounted in high-f granular flows as they are relatively small. For example, kinetic stress is much smaller than contact stress (e.g., Fig. 7), and the kinetic energy associated with velocity fluctuations is much smaller than gravitational potential energy differences in a granular mixture. The results reported here support the premise that, even though velocity fluctuations are relatively small compared with other dynamics in high-f flows, *gradients* of kinetic stress can drive segregation in a wide variety of granular materials at high solids fractions (high f). Specifically, the kinetic stresses drive the segregation direction and magnitude through: (1) the manner in which they are partitioned among different species compared to the partitioning of contact stresses and (2) the gradient in the kinetic stresses. These results are qualitatively similar in mixtures of particles differing only in size and those differing only in density.

A striking difference between the segregation of mixtures of different-sized particles and different density particles in high-f flow is the segregation direction of the more massive particles. The direction of segregation of the more massive (denser) particles in mixtures of particles differing only in density is opposite to the more massive (larger) particles in mixtures of particles differing only in size. In the first case, the more massive (denser) particles segregate along a kinetic stress gradient toward the region of lower kinetic stress, and in the second case, the more massive (larger) particles segregate toward the region of higher kinetic stress. Our results indicate that this difference is driven by the manner in which the kinetic stress is partitioned among the different species. In high-f flows, the smaller particles bear a higher fraction of the kinetic stress than their larger equal-density counterparts [19,29,30,37], and the denser particles bear a higher fraction of the kinetic stress than their lighter equal-sized counterparts (similar to results in Ref. [37]). Previously published results (e.g., Ref. [37]) suggest that these differences are driven primarily by the geometry of correlated particle movements in these high-f flows, so, interestingly, it appears that the geometry driving the fluctuations in these high-f flows is a significant contributor to the segregation in these systems.

Once the kinetic stress is unevenly distributed among the species, the species that bear a larger fraction of the kinetic stress than their volume concentration in the mixture are driven toward "cooler" regions (those of lower kinetic stress and lower granular temperatures). Those that bear a smaller fraction of the kinetic stress are driven toward "hotter" regions (those of higher kinetic stress and higher granular temperatures). It is not immediately obvious why this occurs, but for insight we might consider that all particles appear driven away from high-temperature regions. If one species bears a higher fraction of the kinetic stress than the other, the additional random kinetic energy may allow that species to explore more pore spaces among the mixture to get to the lower-temperature regions.

We have shown here and elsewhere [19,30] that kinetic theory, perhaps the most complete physics-based predictive theoretical framework for granular mixtures, breaks down in its prediction of segregation in high-f flows. While kinetic theory directly accounts for particle scale interactions in the form of transfer of momentum and energy during collisions, the predictions are based on the assumption that collisions are chaotic, uncorrelated, and binary. Effects due to simultaneous multiparticle interactions are typically not captured, though there have been some recent attempts to extend kinetic theory by considering macroscopic structures in granular flows [51]. The need to account for these effects may be responsible for the breakdown in kinetic energy predictions at higher solids fractions. We are currently investigating these questions in detail, as they may also prove relevant for the results we present here where small-scale rearrangements can apparently lead to large-scale system segregation adjustments.

Other than kinetic theory, relatively little theoretical investigation has been performed for the manner in which gradients in velocity fluctations, granular temperature, and kinetic stresses may drive segregation. The theory described here shows promise in its ability to capture segregation in these systems. In the end, it is a relatively simple but critical generalization of the theory presented in Refs. [19,29]. We note that the theory suffers from empirical expressions for drag and diffusion coefficients and other details of the interparticle interactions. In that light, it is interesting to consider the empirical results with those from other models. Most relevant for the mixtures discussed here, Tripathi and Khakhar [27,28] proposed a form for the drag force analagous to Stoke's law. Additionally, the extended form of kinetic theory proposed by Larcher and Jenkins [51] has alternative forms for the drag and diffusion coefficients that could be tested for their effectiveness in application to this mixture theory.

VI. CONCLUSION

In this paper, we performed a numerical and theoretical study of segregation of particles differing only in density sheared in a vertical chute cell. We showed that gradients in the shear rate and associated kinematics in the spanwise direction can drive segregation by particle density in both sparse and high-solids-fraction systems. This shear-induced segregation, reported for high-solids-fraction mixtures of particles differing only in density for the first time, exhibits a similar segregation trend to previous reports of analogous phenomena in sparse flow. Specifically, the denser particles segregate to the region of a lower shear rate and granular temperature, and the less-dense particles segregate to the region of higher shear rate and granular temperature. This is in stark contrast to our previous observations of shear-induced segregation of particles differing only in size [26], which exhibits a phase transition at intermediate concentrations. In sparse flows large particles segregate to regions of low shear rates, low granular temperatures, and low kinetic stress, while in high-solids-fraction flows, large particles segregate to regions of high shear rates, high granular temperatures, and high kinetic stresses. This dichotomy may be related to recent reports of an intermediate segregation state in mixtures of particles differing both in size and density where particles that are both larger and denser than their smaller less dense counterparts rise to an intermediate level in a sheared system where the shear rate is nonuniform (e.g., Refs. [12,52–54]).

Our mixture theory successfully predicts the segregation trends observed in the simulations, though, admittedly, uses empirical fits for some of the coefficients. In the framework of this theory, the shear rate gradients give rise to kinetic stress gradients—closely related to the gradients of granular temperature—which explicitly drive density segregation. Then the particles which bear more of the contact stress than the kinetic stress—here the less-dense particles—are pushed to the regions of low contact stress and high kinetic stress (or high granular temperatures). In contrast, in high-solids-fraction mixtures of particles differing only in size, the large particles bear more of the contact stress than the kinetic stress and push the large particles to the regions of low contact stress and high kinetic stress (or high granular temperature).

Although the framework is reasonable for shear-induced segregation, and predictions appear to correlate reasonably well with observations, a deeper understanding of the kinematics of high-f sheared mixtures is needed for a complete segregation theory. First, we need a relationship between $R_i^c - R_i^k$ and flow properties such as particle concentrations and flow velocities to close the governing equations. For this, we have temporarily used a linear relationship between $R_i^c - R_i^k$ and ϕ_j (for disparate species i and j), though this is clearly not completely representative, judging from the data [Fig. 8(d)]. Coefficients of drag and diffusion also suffer from this empirical oversimplified nature. A more mechanistic way to obtain relationships for D and c_D as they depend on kinematics of the flow is necessary for a predictive model for shear-induced segregation.

Finally, most segregation takes place in a gravitational field where segregation may be driven by simultaneous effects associated with the gravity and shear rate gradients. A more widely applicable theory will combine the theoretical details described in this paper and in Ref. [29] with gravity-driven segregation effects, such as those described by Gray and colleagues, first in Refs. [48,49], or Khakhar and colleagues, first in Ref. [10], and more recently in Refs. [13,27,28]. Preliminary results presented in Ref. [42] show promise in capturing the simultaneous effects of particle size and density in segregating mixtures.

ACKNOWLEDGMENT

We are grateful for the financial support of the National Science Foundation for this project under Grant No. CBET-0932735.

APPENDIX A: KINETIC THEORY EXPRESSIONS USED IN SEGREGATION PREDICTION

As in Refs. [20,23,30], The diffusion velocity of two species i and j in the direction of the interest (e.g., y direction) can be calculated as:

$$v_i - v_j = -\frac{n^2}{n_i n_j} D_{ij} d_i, \qquad \text{(A1)}$$

TABLE IV. Variables in the diffusion equation [Eq. (A1)] of kinetic theory.

Variable	Expression	Description
r_i	r_i	Particle radius of species *i*
m_i	m_i	Particle mass of species *i*
n_i	$\frac{f_i}{4\pi r_i^3/3}$	Number density of species *i*
$T_{D,i}$	$m_i T_i = m_i \frac{\overline{u_i' u_i'}+\overline{v_i' v_i'}+\overline{w_i' w_i'}}{3}$	*Dynamic* granular temperature of species *i*
P_i	$n_i(T_{Di} + \Delta T_{Di}) + \sum_{k=1}^{2} K_{ik}\left[T_{Di} + \frac{(m_i \Delta T_{Dk} + m_k \Delta T_{Di})}{(m_i+m_k)}\right]$	*Dynamic* granular pressure of species *i*
d_i	$d_P + d_T + d_n$	“Diffusion force” for species *i*
d_P	$\frac{\frac{P_i}{P_j}\nabla P_j - \nabla P_i}{nT_D\left(\frac{P_j}{P_i}+1\right)}$	Pressure driven diffusion force
d_T	$-\frac{K_{ij}}{nT_D}\frac{m_j - m_i}{m_j + m_i}$	Thermal driven diffusion force
d_n	$-\frac{K_{ij}}{n}\left[\frac{\nabla n_i}{n_i} - \frac{\nabla n_j}{n_j}\right]$	Ordinary diffusion force
D_{ij}	$\frac{n_i n_j}{n}\frac{r_i + r_j}{K_{ij}}\left[\frac{\pi(m_i+m_j)T_D}{32 m_i m_j}\right]^{1/2}$	Local diffusion coefficient between two species *i* and *j*
K_{ij}	$\left(\frac{\pi}{3}\right) g_{ij} r_{ij}^3 n_i n_j (1+e)$	Coefficient concerning the frequency of interaction
g_{ij}	$\frac{1}{(1-f)} + 6\left(\frac{r_i r_k}{r_i + r_k}\right)\frac{\xi}{(1-f)^2} + 8\left(\frac{r_i r_k}{r_i + r_k}\right)^2 \frac{\xi^2}{(1-f)^3}$	Radial distribution function
ξ	$2\pi(n_i r_i^2 + n_j r_j^2)/3$	Area scale

where D_{ij} is the local coefficient of diffusion and d_i (sometimes called a “diffusion force” [22]) represents competing segregation and mixing factors leading to the difference in diffusion velocities ($v_i - v_j$) and subsequent segregation between the two types of particles. Calculations performed for D_{ij} and d_i are listed in Table IV. The calculations involve terms related to granular temperature T_D, pressure P, and ordinary diffusion represented by d_T,d_p, and d_n. We note that the granular temperature used here is what might be considered a *dynamic* granular temperature compared with the temperature plotted in Fig. 3: $T_{D,i} = m_i T_i$. Also, pressure P_i is distinct from the hydrostatic pressure and is derived from considerations within the framework of kinetic theory and conservation of momentum for the two species as shown in Refs. [20,23].

We average the details in the x and z directions over the first 1 s of the experiment. In our calculations, most of the variables, such as T_D, are calculated directly from the simulations directly, while the initial solids fraction of each species is set to be uniform, each equal to one half of the total solids fraction [$f_i(y) = \langle f \rangle/2$].

The first row of Fig. 11 shows the profiles of $T_D(y)$ for the two constituents at three different $\langle f \rangle$'s. In all systems, T_D is large close to the walls and small at the center of the cell for both species (similar to Fig. 3, row 3). As $\langle f \rangle$ increases from 0.2 to 0.6, temperature gradients decrease approximately by two orders of magnitude. Furthermore, the less dense component always has greater values of T_D than the denser particles in the regions close to the walls, where the flow is dilute [see Fig. 1(d)]. In contrast, T_D are roughly the same in the region at the center of the cell, where the flow is highly concentrated. This matches the observation for the flow of granular mixtures differing only in density in the rotating drums [37]: Granular temperature scales inversely only with size, not with density in high-f regions, while in low-f regions, granular temperature scales inversely with mass (or material density for same-size particles). The second row of Fig. 11 shows profiles of $P(y)$. Similar to T_D, P is large in the region close to the walls and small in the region at the center of the cell. The pressure of less dense particles is larger than dense particles in the dilute region. In the high-f region, the pressure of two species are almost the same.

Figure 12 shows the diffusion forces that drive the segregation and diffusion fluxes (as calculated in Table IV). Based on Eq. (A1), positive (negative) diffusion forces in the left (right) half of the chute cell imply negative (positive) values of $v_l - v_d$, indicating that less-dense particles segregate to the side walls. In all three systems, the thermal “diffusion force,” d_T, that is associated with gradients of the granular temperature is much greater than the other two diffusion forces (i.e., d_n and d_p), indicating that d_T is the *dominating* driving forces for density segregation in vertical chute flow. However, as shown in Fig. 6, the kinetic theory overpredicts $v_l - v_d$ at high f compared with the DEM simulation, which implies that the thermal driven “diffusion force” as calculated in Table IV probably overestimates the granular temperature gradient effects on density segregation in high-f granular flow.

APPENDIX B: STRESS CALCULATION

In this Appendix, we briefly describe our calculations of the total and partial stresses we use for testing our theoretical segregation predictions for the mixture theory. To do so, we divide the chute into equal sized bins in the y direction of width $\Delta y = 2$ mm. We calculate stresses such considering the contribution from the part of each particle j within a bin of width Δy centered at y.

We calculate the kinetic stress $\sigma^{\boldsymbol{k}}_{yy,n}(y) = \rho_n v_n' v_n'(y)$ (the y component of the normal kinetic stress of species n) using a

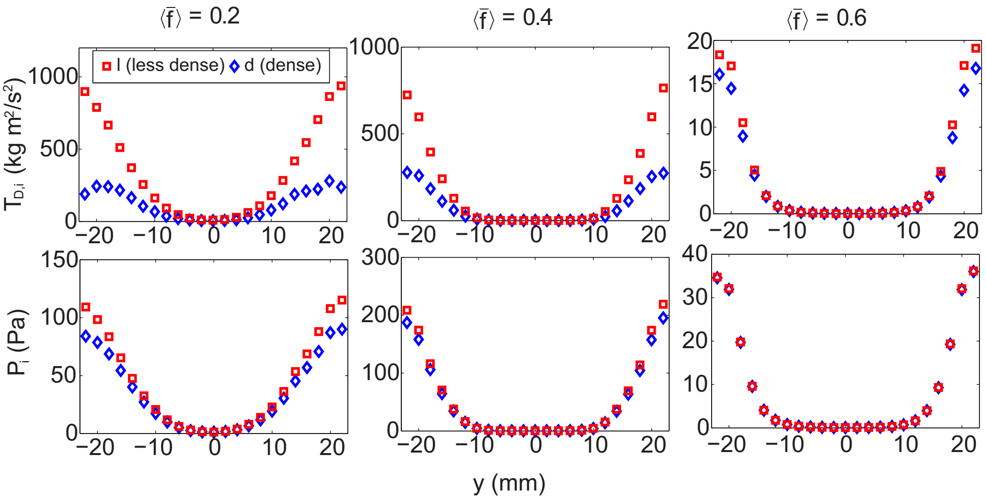

FIG. 11. (Color online) Profiles of dynamic granular temperature and dynamic pressure for two species in the y direction averaged across the width of the chute and over the first 1 s for three systems of different $\langle f\rangle$'s as indicated in the figure. First row: Plots of dynamic granular temperature T_D; second row: Plots of dynamic pressure P.

relatively standard procedure (as in Ref. [29]):

$$\sigma^{\boldsymbol{k}}_{yy,n}(y) = \frac{\rho_{m,n}}{N^2}\left(\sum_{i=1}^{N}\frac{\Sigma_j V_{ij,n}}{V_{\text{bin}}}\right) \times \left\{\sum_{i=1}^{N}\frac{\Sigma_j[v_{ij,n}-v(y)]^2 V_{ij,n}}{\Sigma_j V_{ij,n}}\right\}. \tag{B1}$$

Here i refers to the ith time step of which there are N and j refers to the jth particle (of species n) that is partly or fully in this bin (at time step i). V^n_{ij} and v^n_{ij} are the volume and velocity of that particle, respectively. $V_{\text{bin}} = DL\Delta y$ is the total volume of the bin. $v(y) = \Sigma_n[f^n(y)v^n(y)]/\Sigma_n f^n(y)$ is mean velocity at y. As in Sec. IV B, $\sigma^{\boldsymbol{k}}_{yy}(y) = \Sigma_n \sigma^{\boldsymbol{k}}_{yy,n}(y)$.

To calculate the local contact stress at each position y, we consider each interparticle contact K in a bin of width Δy centered at y. Then we sum the stresses associated with each interparticle contact in each region, as in Refs. [55,56]. Specifically, for the mixture in the y direction, we calculate:

$$\sigma^{\boldsymbol{c}}_{yy}(y) = \frac{\sum_{\tau=1}^{N}\sum_{K=1}^{N_c(y)} F_{ij_K,y}\, l_{ij_K,y}}{N V_{\text{bin}}}. \tag{B2}$$

Here $F_{ij_{K,y}}$ is the force of particle i on particle j associated with the Kth contact in this bin, of which there are $N_c(y,\tau)$ at time step τ. There are N such time steps. $l_{ij_{K,y}}$ is the vector from the center of particle i to the center of particle j.

Since a contact may involve particles of different species, we consider three types of contacts separately in calculating the species contact stresses. (1) Contacts between two less-dense particles only contribute to the partial contact stress of the less-dense particles, and we denote the stress associated Kth such contact as $\boldsymbol{\sigma}^{\boldsymbol{c}}_{K,ll}$. (2) Contacts between two denser particles only contribute to the partial contact stress of the denser particles, and we denote the stress associated Kth such contact as $\boldsymbol{\sigma}^{\boldsymbol{c}}_{K,dd}$. (3) Contacts between one less dense particle and one denser particles contribute to the contact stress of both species; we denote the stress associated Kth such contact as $\boldsymbol{\sigma}^{\boldsymbol{c}}_{K,ld}$. As the size of two species is the same, for each collision between a less-dense and denser particle, we divided the contribution of stress to the partial stresses equally between the two species. Based on that, we calculate the partial contact stress at y for particles of species n at time step τ as:

$$\sigma^{\boldsymbol{c}}_n(y,\tau) = \sum_{K=1}^{N_{c,n}(y)} \sigma^{\boldsymbol{c}}_{K,nn} + \sum_{K=1}^{N_{c,j}(y)} \sigma^{\boldsymbol{c}}_{K,nj}/2. \tag{B3}$$

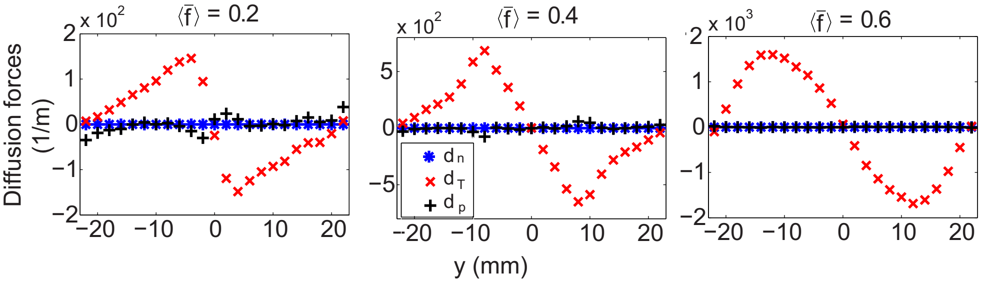

FIG. 12. (Color online) Profiles of driving forces in the y direction averaged across the width of the chute and over the first 1 s for three $\langle f\rangle$'s as indicated in the figure. The three different diffusion forces are d_T, d_p, and d_n vs y.

In this equation, $\sigma^{c}_{K,nn}$ denotes the contact stress associated Kth contact between a particle of type n with another particle of the same species in a bin of width Δy centered at y, of which there are $N^{i}_{c}(y)$. $\sigma^{c}_{K,nj}$ denotes the contact stress associated Kth contact between two particles of different species in a bin of width Δy centered at y, of which there are $N^{j}_{c}(y)$. We calculate the average stress over N time steps:

$$\sigma^{c}_{n}(y) = \sum_{\tau=1}^{N} \sigma^{c}_{n}(y,\tau)/N. \tag{B4}$$

We note that this satisfies $\sigma^{c}(y) = \sigma^{c}_{l}(y) + \sigma^{c}_{d}(y)$, as specified in Sec. IV B.

[1] C. Tai, S. Hsiau, and C. Kruelle, Powder Technol. **204**, 255 (2010).
[2] E. W. C. Lim, AIChE J. **56**, 2588 (2010).
[3] C. Zeilstra, M. A. van der Hoef, and J. A. M. Kuipers, Phys. Rev. E **77**, 031309 (2008).
[4] N. Shishodia and C. R. Wassgren, Phys. Rev. Lett. **87**, 084302 (2001).
[5] J. Saxton, P. Fralick, U. Panu, and K. Wallace, Econ. Geol. **103**, 1657 (2008).
[6] O. Frihy and P. Komar, Mar. Geol. **115**, 253 (1993).
[7] R. Slingerland, Mar. Geol. **47**, 753 (1977).
[8] E. Viparelli, L. Solari, and K. M. Hill, Sedimentology **62**, 1384 (2015).
[9] N. Burtally, P. J. King, and M. R. Swift, Science **295**, 1877 (2002).
[10] D. V. Khakhar, J. J. McCarthy, and J. M. Ottino, Phys. Fluids **9**, 3600 (1997).
[11] K. M. Hill, D. V. Khakhar, J. F. Gilchrist, J. J. McCarthy, and J. M. Ottino, Proc. Natl. Acad. Sci. USA **96**, 11701 (1999).
[12] N. Jain, J. M. Ottino, and R. M. Lueptow, Phys. Rev. E **71**, 051301 (2005).
[13] S. Sarkar and D. V. Khakhar, Europhys. Lett. **83**, 54004 (2008).
[14] L. Sanfratello and E. Fukushima, Granular Matter **11**, 73 (2009).
[15] G. C. Pereira, M. D. Sinnott, P. W. Cleary, K. Liffman, G. Metcalfe, and L. D. Sutalo, Granular Matter **13**, 53 (2011).
[16] N. K. Mitani, H. G. Matuttis, and T. Kadono, Geophys. Res. Lett. **31**, L15606 (2004).
[17] K. M. Hill and Y. Fan, Phys. Rev. Lett. **101**, 088001 (2008).
[18] J. T. Jenkins and D. K. Yoon, Phys. Rev. Lett. **88**, 194301 (2002).
[19] Y. Fan, Shear-induced segregation in dense granular mixtures, Ph.D. thesis, University of Minnesota, 2011.
[20] J. E. Galvin, S. R. Dahl, and C. M. Hrenya, J. Fluid Mech. **528**, 207 (2005).
[21] S. L. Conway, X. Liu, and B. J. Glasser, Chem. Eng. Sci. **61**, 6404 (2006).
[22] J. T. Jenkins and F. Mancini, Phys. Fluids A **1**, 2050 (1989).
[23] D. K. Yoon and J. T. Jenkins, Phys. Fluids **18**, 073303 (2006).
[24] M. Louge and J. Jenkins, in *Mechanics of Deformation and Flow of Particulate Materials* (ASCE, New York, NY, 1997), pp. 370–379.
[25] H. Xu, M. Louge, and A. Reeves, Contin. Mech. Thermodyn. **15**, 321 (2003).
[26] Y. Fan and K. M. Hill, Phys. Rev. Lett. **106**, 218301 (2011).
[27] A. Tripathi and D. V. Khakhar, Phys. Rev. Lett. **107**, 108001 (2011).
[28] A. Tripathi and D. V. Khakhar, J. Fluid Mech. **717**, 643 (2013).
[29] Y. Fan and K. M. Hill, New J. Phys. **13**, 095009 (2011).
[30] Y. Fan and K. M. Hill, Phys. Rev. E **81**, 041303 (2010).
[31] P. A. Cundall and O. D. L. Strack, Geotechnique **29**, 47 (1979).
[32] R. D. Mindlin and H. Deresiewicz, J. Appl. Mech. Trans. ASME **20**, 327 (1953).
[33] Y. Tsuji, T. Tanaka, and T. Ishida, Powder Technol. **71**, 239 (1992).
[34] O. Pouliquen and R. Gutfraind, Phys. Rev. E **53**, 552 (1996).
[35] GDRMiDi, Eur. Phys. J. E **14**, 341 (2004).
[36] V. Chikkadi and M. Alam, Phys. Rev. E **80**, 021303 (2009).
[37] K. M. Hill and J. Zhang, Phys. Rev. E **77**, 061303 (2008).
[38] J. Choi, A. Kudrolli, R. R. Rosales, and M. Z. Bazant, Phys. Rev. Lett. **92**, 174301 (2004).
[39] R. D. Wildman and D. J. Parker, Phys. Rev. Lett. **88**, 064301 (2002).
[40] K. Feitosa and N. Menon, Phys. Rev. Lett. **88**, 198301 (2002).
[41] E. D. Liss, S. L. Conway, and B. J. Glasser, Phys. Fluids **14**, 3309 (2002).
[42] K. Hill and D. S. Tan, J. Fluid Mech. **756**, 54 (2014).
[43] G. K. Batchelor, *An Introduction to Fluid Dynamics* (Cambridge University Press, Cambridge, UK, 2000).
[44] H. Schlichting, *Boundary-Layer Theory* (McGraw-Hill, New York, 1979).
[45] L. W. Morland, J. Geophys. Res. **77**, 890 (1972).
[46] L. W. Morland, Geophys. J. R. Astron. Soc. **55**, 393 (1978).
[47] L. W. Morland, Surv. Geophys. **13**, 209 (1992).
[48] J. M. N. T. Gray and A. R. Thornton, Proc. R. Soc. A **461**, 1447 (2005).
[49] J. M. N. T. Gray and V. A. Chugunov, J. Fluid Mech. **569**, 365 (2006).
[50] Y. Fan, C. P. Schlick, P. B. Umbanhowar, J. M. Ottino, and R. M. Lueptow, J. Fluid Mech. **741**, 252 (2014).
[51] M. Larcher and J. Jenkins, Phys. Fluids **25**, 113301 (2013).
[52] G. Félix and N. Thomas, Phys. Rev. E **70**, 051307 (2004).
[53] J. Zhang and K. M. Hill (unpublished).
[54] K. M. Hill, Y. Fan, J. Zhang, C. Van Niekerk, E. Zastrow, S. C. Hagness, and J. T. Bernhard, Granular Matter **12**, 201 (2010).
[55] C. S. Campbell, J. Fluid Mech. **465**, 261 (2002).
[56] E. Kuhl, G. A. D'Addetta, H. J. Herrmann, and E. Ramm, Granular Matter **2**, 113 (2000).